PHOTONICS Research

Spatially resolved measurement of plasmon dispersion using Fourier-plane spectral imaging

Amir Ohad,[1,2] Katherine Akulov,[2,3] Eran Granot,[3] Uri Rossman,[1] Fernando Patolsky,[3] and Tal Schwartz[2,3,*]

[1]School of Physics, Raymond and Beverly Sackler Faculty of Exact Sciences, Tel Aviv University, Tel Aviv 69978, Israel
[2]Center for Light-Matter Interaction, Tel Aviv University, Tel Aviv 69978, Israel
[3]School of Chemistry, Raymond and Beverly Sackler Faculty of Exact Sciences, Tel Aviv University, Tel Aviv 69978, Israel
*Corresponding author: talschwartz@tau.ac.il

We show that Fourier-plane imaging in conjunction with the Kretschmann–Raether configuration can be used for measuring polariton dispersion with spatial discrimination of the sample, over the whole visible spectral range. We demonstrate the functionality of our design on several architectures, including plasmonic waveguides, and show that our new design enables the measurement of plasmonic dispersion curves of spatially inhomogeneous structures with features as small as 3 μm, in a single shot.   © 2018 Chinese Laser Press

1. INTRODUCTION

Since the discovery of surface plasmon polaritons (SPPs), several techniques have been developed for their excitation and measurement [1,2]. The widely used Kretschmann–Raether prism-coupling configuration is common in most of the current applications of SPPs, primarily in sensing applications and thin film characterization [3]. These techniques rely on the high sensitivity of the surface plasmon resonance to the refractive index of the material in which the plasmons propagate. In order to measure the SPP resonance and its shift under material changes, two approaches are possible—either a broad-spectrum beam is reflected off the metallic surface at a fixed angle (spectral interrogation mode), or a monochromatic collimated beam is used and the reflected intensity is measured, while the angle of incidence is scanned (angular interrogation mode). It was shown in the past that by using Fourier-space (far-field) imaging in conjunction with the Kretschmann–Raether configuration, the two approaches can be unified to obtain the spectral and angular dependence of the plasmon resonance in a single-shot measurement [4–8]. Alternatively, it was recently demonstrated [9] that similar Fourier-plane single-shot measurements can also be achieved by the use of a half-ball prism positioned on top of the sample. These techniques have the advantage that the incident-angle scanning is not done mechanically (which requires a precisely synchronized rotation of both the sample and the detector), but rather optically, taking advantage of the angular decomposition performed by lenses. Therefore, Fourier-plane imaging provides a convenient way to obtain the dispersion curves of surface plasmons over a broad spectral range and to characterize different plasmonic structures, such as periodic arrays or plasmonic waveguides. For sensing applications, it was demonstrated that measuring the reflection as a function of both wavelength and incident angle results in better sensitivity [10,11]. This is because in such a measurement, in comparison to angular or spectral interrogation, more information is obtained and can be fitted numerically to extract refractive-index changes in the sample. Finally, the possibility of measuring the plasmon dispersion in a simple and robust manner can also be used to extract the wavelength-dependent refractive index of an interrogated material, as used in SPP ellipsometry.

Here, we demonstrate that the concept of Fourier-plane imaging can be further expanded to allow for spatially resolved dispersion measurements in planar samples supporting surface plasmons. We show that by shaping the illumination beam and incorporating real-space imaging in the optical setup, pre- and post-selection of the interrogated area can be obtained. Therefore, our new optical design offers hybrid functionality and combines the high sensitivity of the broadband dispersion measurements with the imaging capabilities of surface-plasmon resonance (SPR) imaging techniques. Our measurements show that the lateral detection resolution is high enough to acquire SPP dispersion curves in structures as small as 3 μm.

2. EXPERIMENTAL SETUP

We designed the optical system so as to enable switching between two configurations, as shown in Fig. 1: a normal

real-space imaging mode [Fig. 1(a)] and a Fourier-plane imaging mode [Fig. 1(b)]. We use a fiber-bundle white light source (Olympus, LG-PS2) and pass the light beam through a 70 μm pinhole placed 15 cm after the exit of the fiber bundle. The diffracted beam passes through a linear polarizer, is collimated with a 250 mm lens (L1), and then sent into a right-angle prism (BK7, WZW Optics, RP10) at normal incidence. The sample is attached to the hypotenuse of the prism with immersion oil (refractive index 1.516), and the prism is mounted on a translation stage, allowing the lateral displacement of the sample together with the prism. The diameter of the collimated beam as it enters the prism is approximately 10 mm, and after being reflected from the sample, it is projected by the lenses L2 (focal length 50 mm) and L3 (focal length 75 mm) onto the entrance slit of an imaging spectrometer (Isoplane SCT 320, Princeton Instruments) equipped with a charge-coupled device (CCD) detector (Pixis 1024, Princeton Instruments) and a 50 grooves/mm grating. L2 is positioned such that its front focal plane coincides with the sample, and the spectrometer entrance slit (set to a width of 20 μm) is located at the back focal plane of L3. Therefore, these two lenses form an imaging system with a 1.5× magnification and image the sample onto the entrance plane of the spectrometer. In the imaging mode, we set the angle of the spectrometer grating to 0°, which projects the resulting intermediate image from the plane of the spectrometer entrance slit onto the CCD. Figure 1(c) shows

an image of a 1951 USAF resolution target, as recorded in the real-space imaging mode with the spectrometer slit removed. As can be seen, the spatial resolution of the imaging is sufficient for imaging features smaller than 8 μm.

In order to switch to the Fourier-plane imaging mode [Fig. 1(b)], we first insert a cylindrical lens (C1, focal length 50 mm) before the prism, which focuses the beam into a narrow horizontal strip of 14 μm full width at half-maximum (FWHM), exactly on the sample, as shown in Fig. 1(d). With this, we achieve two goals—first, as also used in Refs. [4–8], the sample is simultaneously probed by many plane waves making up the converging beam and having an angular span of 10° (in air). Using Snell's law, this is translated to a range of incident angles of 41°–48° with respect to the sample. Second, by probing the sample with a focused beam, we obtain spatial localization of 20 μm of the interrogated area in the vertical dimension (taking into account the 45° tilt of the sample). The spectrometer slit, set to a 20 μm width, provides us with lateral localization of 13.3 μm (due to the 1.5× magnification of the imaging system), as it post-selects only a small section of the illuminated area of the sample. Therefore, by limiting the interrogated area both in the vertical and horizontal directions, we can obtain a local measurement of the dispersion. We stress that, since the spatial localization is achieved in different manners for the horizontal and vertical dimensions, and on different stages of the imaging setup, we avoid the risk of mixing between the two dimensions, which might occur if one used a spherical lens to focus the light onto the sample, instead of the cylindrical lens C1. To perform the optical Fourier transform, a negative cylindrical lens (C2, focal length −30 mm) is placed after the prism, such that a plane wave entering C2 is transformed into a virtual image of a horizontal line, located behind C2. This virtual horizontal line is displaced from the optical axis (in the vertical direction) by a distance that depends on the entrance angle of the plane wave into C2. We adjust the exact position of C2 by bringing this virtual image to coincide with the plane of the sample, such that the thin horizontal line is refocused at the slit by the L2–L3 lens pair, as seen in Fig. 1(e). In that way, the spectrometer images the Fourier plane of C2, which corresponds to the angular distribution along the vertical (y) direction. As the angular span of the light beams around the optical axis is small (±4°), we can use the paraxial approximation to relate the vertical position on the CCD with the propagation angle (θ_a) of a plane wave entering C2 by

$$y = y_0 + 1.5 \times f_{C2} \sin \theta_a, \tag{1}$$

where y_0 corresponds to the intersection between the optical axis and the CCD, and we have taken into account the 1.5× magnification of the imaging lenses. Furthermore, denoting the incident angle of the light inside the prism (with respect to the normal to the sample) by θ_i and using Snell's law, this angle is given by the relation

$$\theta_i = 45° + \arcsin\left(\frac{1}{n_p} \sin \theta_a\right), \tag{2}$$

with $n_p = 1.5$ being the refractive index of the BK7 prism. Note that the width of the focused beam in the Fourier plane [see Fig. 1(e)] is 9 μm FWHM, meaning that the angular resolution of our measurement is 0.7 arcmin. Finally, the
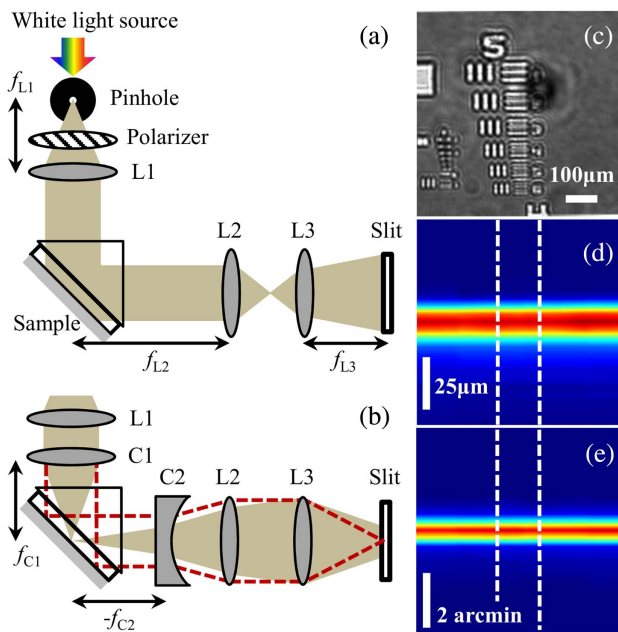

Fig. 1. Schematic sketch of the measurement system (a) in real-space imaging mode and (b) in Fourier-plane imaging mode. The dashed red lines illustrate the evolution of a single plane wave entering the prism and propagating through the setup in Fourier-plane imaging mode. (c) A subsection of a resolution target, as imaged through the optical system in the real-space imaging mode. (d) Real-space intensity distribution at the sample plane after focusing by L1. (e) Intensity distribution in Fourier-plane imaging mode for an incoming collimated beam. The dashed vertical lines in (d) and (e) mark the edges of the spectrometer entrance slit.

spectrometer disperses the various wavelengths contained in the white light beam along the horizontal direction (x), and thus we obtain a full mapping of the angle-resolved reflection spectrum of the sample, in a similar manner to Ref. [8]. Note that for all the lenses besides C2, we use achromatic doublets in order to avoid chromatic aberrations. In addition, the cylindrical lenses C1 and C2 are mounted on a flip-mount to allow a convenient and reproducible removal and insertion of the lenses to switch between the real-space and Fourier-space imaging modes. This convenient switching between different imaging modes provides us with the ability to accurately select the interrogated area within the sample, as we demonstrate below (see Section 4).

Compared to all previous work, the main strength of our configuration is that it allows the acquisition of the plasmonic dispersion relation with spatial discrimination and a resolution of several micrometers. This advantage stems from the combination of an imaging system (formed by L2 and L3) and 1D Fourier imaging by C2, along with the pre-selection of the illuminated area by C1 and the post-selection of the measured area by the spectrometer slit. Moreover, the use of a negative lens (C2) to perform the optical Fourier transform ensures that the length of the optical path is minimal, resulting in a higher numerical aperture for given lens sizes. With the specific choice of parameters used, our setup provides us with the ability to measure the dispersion over an area as small as 13.3 μm × 20 μm. In principle, the interrogated area can be made even smaller, by using a stronger lens for C1, or higher magnification in the imaging subsystem. Alternatively, reducing the pinhole size or the width of the spectrometer entrance slit will also result in better spatial discrimination, but this will come at the expense of intensity and signal-to-noise ratio (SNR). We note that similar spatial discrimination can also be obtained by imaging the sample onto an intermediate plane and placing an aperture that selects a small area of the resulting image. However, in this manner, most of the light will be blocked, resulting in a weaker signal and lower sensitivity. Moreover, the additional imaging stage will require further alignment and may increase the effect of aberrations.

In the Kretschmann configuration, the resonance angle for each wavelength is determined by momentum conservation between the SPP propagating along the film and the plane wave impinging on the sample through the prism. This condition is expressed by

$$k_{spp} = k_0 n_p \sin \theta_i, \qquad (3)$$

where $k_0 = 2\pi/\lambda = \omega/c$ is the wavenumber in vacuum, λ is the wavelength of light, ω is the angular frequency and c is the speed of light. Using this expression, the dispersion relation $\omega(k_{spp})$ can be extracted from the measurement. Alternatively, and as will be used below, the SPP dispersion relation can be presented in terms of the wavelength-dependent effective index for the plasmon propagating along the interface, which is defined by

$$n_{eff} = \frac{k_{spp}}{k_0} = n_p \sin \theta_i. \qquad (4)$$

Using Eqs. (1)–(4), one finds that in our setup, the effective index of refraction can be related to the vertical position on the CCD using

$$n_{eff} = n_p \sin \left[45° + \arcsin \left(\frac{1}{n_p} \times \frac{y - y_0}{1.5 f_{C2}} \right) \right]. \qquad (5)$$

In order to determine the value of y_0, we remove the focusing lens C1, which results in a single plane wave being reflected from the sample at 45°, propagating parallel to the optical axis and finally focused at the Fourier plane [as shown in Fig. 1(e)]. This calibration procedure was performed before each set of measurements in order to compensate for small misalignments of the system. Spectral calibration was performed using a mercury-vapor discharge lamp.

3. PLASMON DISPERSION ON PLANAR FILMS

First, we tested the performance of our setup on a simple planar Ag film. The sample was fabricated by sputtering a 50 ± 2 nm layer of Ag on a glass substrate. In order to obtain normalized reflection maps, we initially measured the sample with transverse electric (TE) polarized light, for which no plasmons are excited, and the reflectivity of the Ag film depends weakly on either the wavelength or the angle of incidence. Figure 2(a) shows the resulting reflected intensity map as a function of wavelength (horizontal axis) and position y (vertical axis). We then rotated the polarizer and repeated the measurement with transverse magnetic (TM) polarization [Fig. 2(b)]. By taking the ratio of these two images, we obtain a normalized reflectivity map, and using Eq. (5), we transformed the resulting image to obtain the plasmonic dispersion $n_{eff}(\lambda)$, which is clearly visible as a dark notch in Fig. 2(c). We obtained good SNRs throughout the spectral range of 420–850 nm and an
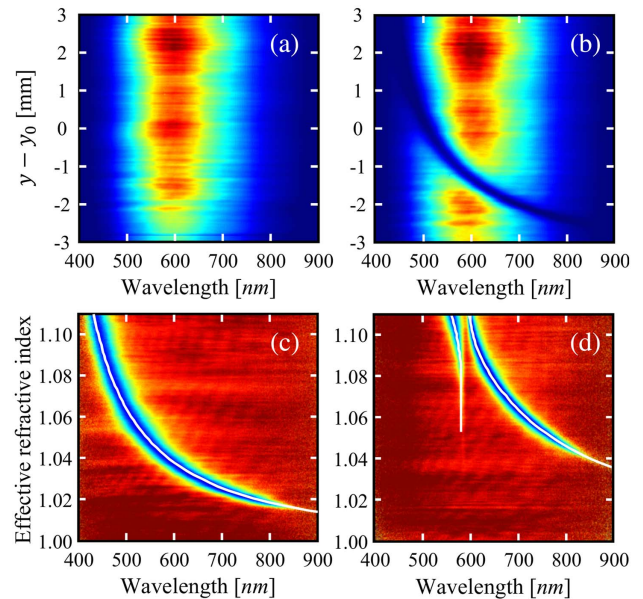
Fig. 2. Reflected intensity maps recorded for an Ag film for (a) TE and (b) TM polarizations. (c) Dispersion diagram of the SPP on an Ag film, measured by Fourier-plane spectral imaging. The solid line shows the SPP dispersion curve calculated by the T-matrix method. (d) Measured dispersion curve for an Ag film covered with a PVA/TDBC layer, exhibiting normal-mode splitting as a result of strong coupling between SPPs and molecular excitons. The solid lines show the dispersion curve calculated by the T-matrix method with the PVA thickness and the molecular absorption as free parameters.

effective index range of 1–1.11. This range is limited by the numerical aperture of the system and can be increased by the use of larger lenses. The white solid line superimposed on the image corresponds to the theoretical dispersion curve of an SPP propagating on the Ag–air interface, which was calculated using transfer-matrix simulations (with the dielectric function of Ag measured by ellipsometry). Our measurement exhibits excellent agreement with the numerical simulations throughout the whole spectral range, confirming the accuracy of our measurement technique.

As another example of the capabilities of the Fourier-plane imaging technique, we used our setup to measure the dispersion of exciton-plasmon polaritons [12–15], formed by the strong coupling of surface plasmons to thin films of organic dye molecules. For this purpose, we prepared a sample composed of a 50-nm-thick Ag film on which we spin-coated a thin layer of a transparent polyvinyl alcohol (PVA) polymer doped with TDBC molecules (5,6-dichloro-2-[[5,6-dichloro-1-ethyl-3-(4-sulphobutyl)benzimidazol-2-ylidene]propenyl]-1-ethyl-3-(4-sulphobutyl) benzimidazolium hydroxide, inner salt, sodium salt) (Few Chemicals, S0046). These molecules form J-aggregates that have a sharp absorption peak at 590 nm, and they were previously used for studying strong light–matter coupling in both plasmonic and microcavity systems [12,16,17]. Under strong coupling conditions, when the dispersion curve of the electromagnetic modes crosses the molecular absorption, the dispersion splits into two separate curves known as the upper and lower polariton branches. The behavior is clearly observed in Fig. 2(d), which shows the dispersion measured in a similar manner as for the bare silver film. Around the exciton-plasmon resonance, we find a splitting of 130 meV, which is within the typical range of values measured previously. Note that, as expected, the plasmonic dispersion is pushed toward higher effective indices, due to the presence of the high-index PVA layer on top of the Ag film. Once again, we compared the experimental measurement to numerical simulations, which are represented by the solid lines in Fig. 2(d). In these simulations, the thickness of the PVA layer (taken with a refractive index of 1.5) was adjusted by fitting the calculated dispersion to the measured one. Using this fitting procedure, we found that the PVA/TDBC layer has a thickness of 20 nm and an absorbance of 0.08 at the exciton wavelength (590 nm).

4. DISPERSION OF PLASMONIC WAVEGUIDES

In the two former examples, the measured structures were spatially homogeneous. However, as we designed our measurement system to have spatial discrimination capabilities, we can use it to perform local dispersion measurements on inhomogeneous samples. In order to demonstrate this unique functionality, we fabricated a series of several plasmonic metal-strip waveguides [2,18], which support propagation of surface plasmons along the waveguides. Similar structures were previously measured using leakage-radiation microscopy [19,20], and here we show that such structures can also be measured using our method, which is compatible with standard SPR-sensing configurations. Figure 3(a) shows a microscope image of the array, which consists of 200-μm-long metal-strip waveguides with
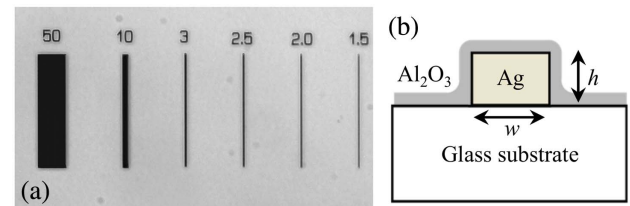

Fig. 3. (a) Optical microscope image of the fabricated metal-strip waveguides. The numbers indicate the widths of the individual waveguides. (b) A schematic sketch of a waveguide cross section.

varying width ($w = 50$, 10, 3, 2.5, 2, and 1.5 μm). In addition, we fabricated on the same sample a square Ag patch of 200 μm × 200 μm, emulating a homogeneous metal film. This sample was fabricated using e-beam lithography, followed by evaporation of $h = 50$-nm-thick Ag layer. Finally, in order to protect the Ag film from oxidation, we deposited a thin layer of Al_2O_3 using atomic-layer deposition (ALD). A sketch of the resulting waveguide structure is shown in Fig. 3(b). In order to measure the different waveguides, we switched our setup to imaging mode by removing lenses C1 and C2 and aligned the sample such that a particular waveguide is located at the center of the field of view, with its image coinciding with the spectrometer entrance slit. The system was then switched back to the Fourier-imaging mode in order to measure the dispersion curve of the individual waveguides. The reflection reference used for the waveguide-array sample was recorded by measuring an area in between the waveguides (glass covered by Al_2O_3), in TM polarization.

In Figs. 4(a)–4(d) we plot the results of the Fourier-plane imaging measurement, taken for the 200 μm square patch
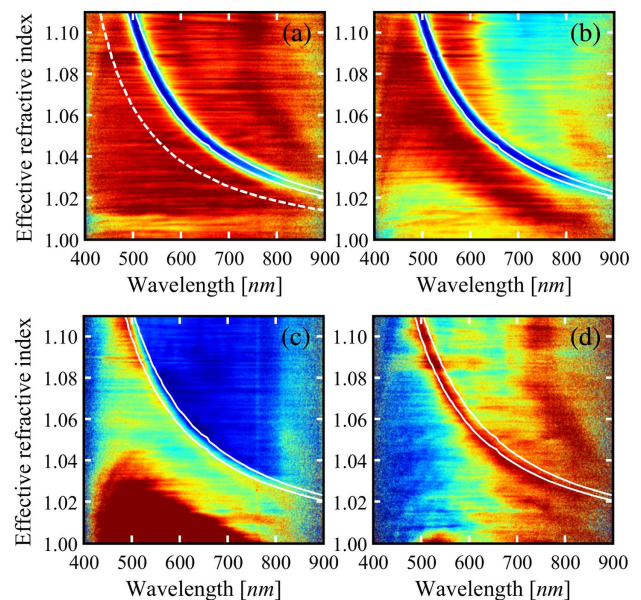

Fig. 4. SPP dispersion measured by Fourier-plane spectral imaging (a) for a 200 μm × 200 μm Ag patch covered with Al_2O_3 and for metal-strip waveguides of widths (b) $w = 50$ μm, (c) $w = 10$ μm, and (d) $w = 3$ μm. The solid lines correspond to the simulated dispersion with an Al_2O_3 layer in the range of 7.5–10 nm, and the dashed line in (a) corresponds to the dispersion curve calculated for a bare Ag film.

[Fig. 4(a)] and for waveguides with a width of 50, 10, and 3 μm [Figs. 4(b)–4(d)]. The dispersion curve of the SPP is clearly seen for all of the waveguides, which demonstrates our ability to measure the dispersion locally, down to structures as small as 3 μm. For the narrower waveguides, the images were too blurred to identify the plasmonic dispersion. In order to validate the results in Fig. 4, we compared them to our numerical simulations. Note that for waveguide widths of several micrometers or more, the plasmonic dispersion barely changes as a result of the lateral confinement [21], making it practically identical to the dispersion of plasmons propagating on a uniform surface. Moreover, as the reflected field is uniform across the width of the waveguides, it cannot couple to high-order plasmonic modes [21], and only a single branch is seen in the measurements. This permits us to use the same transfer matrix simulations as in Section 3, with the addition of the thin Al_2O_3 layer on top of the Ag film. Moreover, by fitting the results of the simulations to the measured dispersion curves, we are able to extract the thickness of the Al_2O_3 layer. The dashed line in Fig. 4(a) corresponds to the SPP dispersion calculated for an Ag–air interface, as in Fig. 2(c), whereas the solid lines are the dispersion curves calculated for the Ag layer covered with a layer of 7.5 nm and 10 nm thick Al_2O_3, respectively. As seen in Fig. 4(a), the measured dispersion is well situated between these two lines over the whole spectral range between 500 nm and 850 nm, resulting in a thickness-sensing resolution better than 1.5 nm. As previously demonstrated, by using more sophisticated spectral fitting methods [11,22], a further increase in accuracy can be obtained when extracting optical properties from complete dispersion curves. For the waveguide structures [Figs. 4(b)–4(d)], we plot the same two simulated curves and find that the measured SPP dispersion curves still lie within the same error margins, meaning that the sensing capabilities are maintained even for the measurement over the smallest structure of 3 μm. Therefore, our results indicate that the Fourier-plane imaging setup with our new design can be used for high-resolution sensing applications, with a spatial resolution of several micrometers.

It is interesting to note that in Figs. 4(a) and 4(b), corresponding to relatively large widths, the plasmon dispersion appears as a dark notch in the reflectivity map, which is normal for Kretschmann–Raether measurements. However, for waveguide widths of 10 μm and less, the same dispersion curve appears as a signal higher than the background, even though it has the same shape. We suspect that this is a result of diffraction effects, which arise when the width of the waveguide is comparable to the spatial resolution limit of the imaging system. For such small structures, part of the light will not be collected and re-focused on the spectrometer entrance slit, resulting in a reflection baseline lower than 100%, as for a planar, homogeneous film; however, waves that fall on the plasmon dispersion curve are coupled to the waveguide, and therefore such scattering losses are weaker.

In conclusion, we presented a new optical design that is based on the Kretschmann–Raether configuration and incorporates both Fourier-plane spectral imaging and real-space imaging as a convenient platform for performing spatially resolved, single-shot measurements of plasmonic dispersion curves. We demonstrated the measurement of SPP dispersion on bare planar Ag films and SPP waves strongly coupled to molecular films, over a broad spectral range of 420–850 nm. Taking advantage of the spatial-interrogation capabilities, we measured the SPP dispersion curves of metal-strip waveguides and demonstrated that our method allows local measurement of waveguides that are as narrow as 3 μm. Like previous Fourier-space imaging methods used for dispersion measurements [4–9], our method can be used for broadband, high-resolution, and real-time sensing applications. However, in addition, it permits spatial discrimination of several micrometers and mapping of spatially inhomogeneous structures, using lateral scanning over the interrogated area. As such, our new method stands in the gap between conventional SPR sensors, which provide high sensing resolution, and plasmon imaging techniques, such as leakage-radiation microscopy [19,20,23,24] or scanning near-field microscopy, which provide high spatial resolution, but require elaborate optical setups and precise alignment. Finally, we stress that in our system, as with other prism-based configurations, the angular span of the excitation beam is relatively narrow and matches the momentum range of the plasmonic modes. In comparison to leakage-radiation microscopy, where the angular spread of the focused beam is very broad (corresponding to the full aperture of the focusing objective), our method provides maximal coupling of light into surface plasmons, and therefore higher SNR and higher sensitivity.

REFERENCES

1. H. Raether, *Surface Plasmons on Smooth and Rough Surfaces and on Gratings,* Springer Tracts in Modern Physics (Springer Berlin Heidelberg, 1988), Vol. **111**.
2. S. A. Maier, *Plasmonics: Fundamentals and Applications* (Springer, 2007), Vol. **58**.
3. J. Homola, "Surface plasmon resonance sensors for detection of chemical and biological species," Chem. Rev. **108**, 462–493 (2008).
4. J. D. Swalen, J. G. Gordon, M. R. Philpott, A. Brillante, I. Pockrand, and R. Santo, "Plasmon surface polariton dispersion by direct optical observation," Am. J. Phys. **48**, 669–672 (1980).
5. S. C. Kitson, W. L. Barnes, G. W. Bradberry, and J. R. Sambles, "Surface profile dependence of surface plasmon band gaps on metallic gratings," J. Appl. Phys. **79**, 7383–7385 (1996).
6. C. H. Park, J. W. Choi, and Y.-H. Cho, "Real-time surface plasmon resonance dispersion imaging with a wide range of incident angles and detection wavelengths," Appl. Opt. **49**, 2470–2474 (2010).
7. C. J. Alleyne, P. J. R. Roche, S. Filion-Côté, and A. G. Kirk, "Analysis of surface plasmon spectro-angular reflectance spectrum: real-time measurement, resolution limits, and applications to biosensing," Opt. Lett. **36**, 46–48 (2011).
8. M. Ives, T. M. Autry, S. T. Cundiff, and G. Nardin, "Direct imaging of surface plasmon polariton dispersion in gold and silver thin films," J. Opt. Soc. Am. B **33**, C17–C21 (2016).
9. R. Dehmel, J. J. Baumberg, U. Steiner, and B. D. Wilts, "Spectrally resolved surface plasmon resonance dispersion using half-ball optics," Appl. Phys. Lett. **111**, 201102 (2017).
10. Z. Qi, M. Wei, H. Matsuda, I. Honma, and H. Zhou, "Broadband surface plasmon resonance spectroscopy for determination of refractive-index dispersion of dielectric thin films," Appl. Phys. Lett. **90**, 181112 (2007).

11. S. Filion-Côté, P. J. R. Roche, A. M. Foudeh, M. Tabrizian, and A. G. Kirk, "Design and analysis of a spectro-angular surface plasmon resonance biosensor operating in the visible spectrum," Rev. Sci. Instrum. **85**, 093107 (2014).

12. J. Bellessa, C. Bonnand, J. C. Plenet, and J. Mugnier, "Strong coupling between surface plasmons and excitons in an organic semiconductor," Phys. Rev. Lett. **93**, 036404 (2004).

13. T. Schwartz, J. A. Hutchison, C. Genet, and T. W. Ebbesen, "Reversible switching of ultrastrong light-molecule coupling," Phys. Rev. Lett. **106**, 196405 (2011).

14. P. Törmä and W. L. Barnes, "Strong coupling between surface plasmon polaritons and emitters: a review," Rep. Prog. Phys. **78**, 013901 (2015).

15. T. W. Ebbesen, "Hybrid light-matter states in a molecular and material science perspective," Acc. Chem. Res. **49**, 2403–2412 (2016).

16. J. R. Tischler, M. Scott Bradley, Q. Zhang, T. Atay, A. Nurmikko, and V. Bulović, "Solid state cavity QED: strong coupling in organic thin films," Org. Electron. **8**, 94–113 (2007).

17. T. Schwartz, J. A. Hutchison, J. Leonard, C. Genet, S. Haacke, T. W. Ebbesen, and J. Léonard, "Polariton dynamics under strong light-molecule coupling," ChemPhysChem **14**, 125–131 (2013).

18. W. L. Barnes, A. Dereux, and T. W. Ebbesen, "Surface plasmon sub-wavelength optics," Nature **424**, 824–830 (2003).

19. S. Massenot, J. Grandidier, A. Bouhelier, G. Colas des Francs, L. Markey, J.-C. Weeber, A. Dereux, J. Renger, M. U. Gonzàlez, and R. Quidant, "Polymer-metal waveguides characterization by Fourier plane leakage radiation microscopy," Appl. Phys. Lett. **91**, 243102 (2007).

20. H. Yang, M. Qiu, and Q. Li, "Identification and control of multiple leaky plasmon modes in silver nanowires," Laser Photon. Rev. **10**, 278–286 (2016).

21. R. Zia, M. D. Selker, and M. L. Brongersma, "Leaky and bound modes of surface plasmon waveguides," Phys. Rev. B **71**, 165431 (2005).

22. C. J. Alleyne, A. G. Kirk, W.-Y. Chien, and P. G. Charette, "Numerical method for high accuracy index of refraction estimation for spectro-angular surface plasmon resonance systems," Opt. Express **16**, 19493–19503 (2008).

23. A. Drezet, A. Hohenau, D. Koller, A. Stepanov, H. Ditlbacher, B. Steinberger, F. R. Aussenegg, A. Leitner, and J. R. Krenn, "Leakage radiation microscopy of surface plasmon polaritons," Mater. Sci. Eng. B **149**, 220–229 (2008).

24. A. Hohenau, J. R. Krenn, A. Drezet, O. Mollet, S. Huant, C. Genet, B. Stein, and T. W. Ebbesen, "Surface plasmon leakage radiation microscopy at the diffraction limit," Opt. Express **19**, 25749–25762 (2011).